

THE SPECTRAL ENERGY DISTRIBUTIONS OF WHITE DWARFS IN 47 TUCANAE: THE DISTANCE TO THE CLUSTER

K. A. WOODLEY¹, R. GOLDSBURY¹, J. S. KALIRAI^{2,3}, H. B. RICHER¹, P.-E. TREMBLAY⁴, J. ANDERSON², P. BERGERON⁵, A. DOTTER², L. ESTEVES⁶, G. G. FAHLMAN⁷, B. M. S. HANSEN⁸, J. HEYL¹, J. HURLEY⁹, R. M. RICH⁸, M. M. SHARA¹⁰, P. B. STETSON⁷

Draft version November 5, 2018

ABSTRACT

We present a new distance determination to the Galactic globular cluster 47 Tucanae by fitting the spectral energy distributions of its white dwarfs to pure hydrogen atmosphere white dwarf models. Our photometric dataset is obtained from a 121 orbit Hubble Space Telescope program using the Wide Field Camera 3 UVIS/IR channels, capturing F390W, F606W, F110W, and F160W images. These images cover more than 60 arcmin² and extend over a radial range of 5 – 13.7 arcmin (6.5 – 17.9 pc) within the globular cluster. Using a likelihood analysis, we obtain a best fitting unreddened distance modulus of $(m - M)_0 = 13.36 \pm 0.02 \pm 0.06$ corresponding to a distance of $4.70 \pm 0.04 \pm 0.13$ kpc, where the first error is random and the second is systematic. We also search the white dwarf photometry for infrared excess in the F160W filter, indicative of debris disks or low mass companions, and find no convincing cases within our sample.

Subject headings: Galaxy: globular clusters: individual(47 Tucanae) — white dwarfs — stars: distances

1. INTRODUCTION

Many astrophysical analyses involving globular clusters rely on well determined metallicity, reddening, and distance measurements. In particular, the estimated ages of Galactic globular clusters can depend heavily on these assumed quantities, so their careful determination is necessarily important. Ages of Galactic globular clusters can place strong constraints on the epoch of formation of our Galaxy, identify when cluster formation occurred with respect to the era of reionization in the Universe and the cosmic star formation peak, constrain the formation history of the Galaxy by dating the halo and bulge, as well as constrain Ω_M (Gratton et al. 2003) when coupled with

measurements of H_0 by WMAP (Spergel et al. 2003) and the HST Key Project (Freedman et al. 2001). Most of the Galactic globular clusters have ages between 9-14 Gyr (e.g. Marin-Franch et al. 2009; Dotter et al. 2010), with most absolute ages commonly determined by fitting theoretical isochrones to the main sequence turnoff. This, however, depends strongly on the assumed distance modulus to the cluster, which is the most significant contributor to the age uncertainty (Bolte & Hogan 1995). Although less sensitive to distance, even the more recently employed age dating technique via the white dwarf cooling sequence (Hansen et al. 2004, 2007) requires a precise distance modulus.

The Galactic globular cluster 47 Tucanae (47 Tuc, NGC 104) is considered the metal-rich proto-type for globular cluster work ($[\text{Fe}/\text{H}] = -0.74 \pm 0.003 \pm 0.026$, Carretta et al. 2009). As the closest and least reddened metal-rich globular cluster, 47 Tuc serves as an important science, as well as a calibration target, for the Hubble Space Telescope (HST). It is used as a metal-rich anchor when comparing observations of resolved stars in nearby galaxies to stellar evolutionary models (Cassisi & Salaris 1997; Zoccali et al. 1999; Ferraro et al. 1999; Di Cecco et al. 2010) and in examining the star formation history of galaxies in the Local Group (e.g. Monelli et al. 2010). As another example, the Wide Field Camera 3 (WFC3) Galactic Bulge Treasury program (GO-11664) has targeted 47 Tuc in their resolved stellar population study (Brown et al. 2009). With these observations, ranging from the UV to near-IR, 47 Tuc will serve as an empirical population template, helping to calibrate the reddening-free indices and correcting the transformation of theoretical isochrone libraries into the WFC3 photometric system.

With relatively well measured values of metallicity and reddening ($E(B - V) = 0.04 \pm 0.02$, Salaris et al. 2007; Harris 2010), the distance becomes the crucial input parameter to determine the age of 47 Tuc. A

¹ Department of Physics & Astronomy, University of British Columbia, Vancouver, BC, Canada V6T 1Z1; kwoodley@phas.ubc.ca, rgoldsb@phas.ubc.ca, richer@astro.ubc.ca, heyl@phas.ubc.ca

² Space Telescope Science Institute, 3700 San Martin Drive, Baltimore, MD, 21218; jkalirai@stsci.edu, jayander@stsci.edu, dotter@stsci.edu

³ Center for Astrophysical Sciences, Johns Hopkins University, Baltimore, MD, 21218

⁴ Zentrum für Astronomie der Universität Heidelberg, Landessternwarte, Königstuhl 12, 69117 Heidelberg, Germany; ptremblay@lsw.uni-heidelberg.de

⁵ Département de Physique, Université de Montréal, C.P. 6128, Succ. Centre-Ville, Montréal, Québec H3C 3J7, Canada; bergeron@astro.umontreal.ca

⁶ Department of Physics, University of Guelph, Guelph, ON, Canada N1G 2W1; lesteves@uoguelph.ca

⁷ National Research Council, Herzberg Institute of Astrophysics, Victoria, BC, Canada V9E 2E7; greg.fahlgman@nrc-cnrc.gc.ca, peter.stetson@nrc-cnrc.gc.ca

⁸ Division of Astronomy and Astrophysics, University of California at Los Angeles, Los Angeles, CA, 90095; hansen@astro.ucla.edu, rmr@astro.ucla.edu

⁹ Centre for Astrophysics & Supercomputing, Swinburne University of Technology, Hawthorn, VIC 3122, Australia; jhurley@swin.edu.au

¹⁰ Department of Astrophysics, American Museum of Natural History, Central Park West and 79th Street, New York, NY 10024; mshara@amnh.org

TABLE 1
COMPARATIVE ABSOLUTE DISTANCE ESTIMATES TO 47 Tuc

$(m - M)_o^a$	Method	Reference
$13.36 \pm 0.02 \pm 0.06^b$	WD Spectral Energy Distributions	This Paper
13.23 ± 0.08	Eclipsing Binary	Thompson et al. (2010)
13.25	Main Sequence Fitting	Bergbusch & Stetson (2009)
13.32 ± 0.09	Tip of the Red Giant Branch	Bono et al. (2008)
13.47 ± 0.11	RR Lyrae	Bono et al. (2008)
13.28 ± 0.07	Eclipsing Binary	Kaluzny et al. (2007)
$13.18 \pm 0.03 \pm 0.04^b$	Horizontal Branch Fitting	Salaris et al. (2007)
13.02 ± 0.19	Cluster Kinematics	McLaughlin et al. (2006)
$13.40 \pm 0.08^{c,d}$	Main Sequence Fitting	Gratton et al. (2003)
$13.25 \pm 0.06 \pm 0.07$	Main Sequence Fitting	Percival et al. (2002)
$13.21 \pm 0.04 \pm 0.07^b$	Main Sequence Fitting	Grundahl et al. (2002)
13.15 ± 0.14	WD Cooling Sequence Fitting	Zoccali et al. (2001)
13.45 ± 0.09^c	Main Sequence Fitting	Carretta et al. (2000)
13.32 ± 0.20	Tip of the Red Giant Branch	Ferraro et al. (2000)
13.29 ± 0.20^e	Horizontal Branch Fitting	Ferraro et al. (1999)
13.57 ± 0.15	Main Sequence Fitting	Reid (1998)
$13.32 \pm 0.03 \pm 0.04^b$	Horizontal Branch Fitting	Kaluzny et al. (1998)
13.23 ± 0.17	Baade-Wesselink of RR Lyrae	Storm et al. (1994)
13.38 ± 0.05	Horizontal Branch Fitting	Salaris & Weiss (1998)
13.52 ± 0.08^c	Main Sequence Fitting	Gratton et al. (1997)
13.28	Horizontal Branch Fitting	Hesser et al. (1987)
13.18	Main Sequence Fitting	Hesser et al. (1987)

^a Dereddened using $E(B - V) = 0.04$ and $A_V / E(B - V) = 3.1$.

^b The first uncertainty is random and the second is systematic.

^c Derived from the quoted distance modulus uncorrected for binary bias. A binary correction removes 0.02 mag from the distance modulus.

^d Using their mean distance derived from two colors.

^e From their global metallicity derived distance modulus.

considerable effort has gone into determining the distance to this cluster. We list recent work in Table 1. There has been quite a variety of methodologies used to determine the distance of this cluster, including main sequence fitting (Hesser et al. 1987; Gratton et al. 1997; Reid 1998; Carretta et al. 2000; Grundahl et al. 2002; Percival et al. 2002; Gratton et al. 2003; Bergbusch & Stetson 2009), the tip of the red giant branch (Ferraro et al. 2000; Bono et al. 2008), horizontal branch fitting (Hesser et al. 1987; Kaluzny et al. 1998; Salaris & Weiss 1998; Ferraro et al. 1999; Salaris et al. 2007), RR Lyrae (Storm et al. 1994; Bono et al. 2008), cluster stellar kinematics (McLaughlin et al. 2006), eclipsing binaries (Kaluzny et al. 2007; Thompson et al. 2010), and white dwarf (WD) cooling sequence fitting (Zoccali et al. 2001). This set of measurements spans unreddened distance moduli between $13.02 - 13.57$ for 47 Tuc which has important implications for the derived age. Examining only the main sequence turnoff luminosity for a cluster at the extremes in distance moduli, this yields a difference in age of ~ 6 Gyr¹¹, altering any inferred history of the formation of the Milky Way that one might derive from 47 Tuc.

Our goal is to determine the distance to 47 Tuc following the example of Zoccali et al. (2001) by using the cluster's WD population. Zoccali et al. (2001) constructed a WD sequence using local calibrators with measured trigonometric parallaxes and magnitudes to com-

pare with the WD cooling sequence of 47 Tuc, yielding an unreddened distance modulus of $(m - M)_o = 13.15 \pm 0.14$ (see Table 1). Here, rather than use local calibrators, we determine the distance by comparing our measured photometry to the hydrogen atmosphere (DA) WD models of Tremblay et al. (2011) and the helium atmosphere (DB) models of Bergeron et al. (2011). Previous spectroscopic studies have found solely DA WDs in globular clusters within the temperature range of our sample, including the globular clusters M4 (Davis et al. 2009), NGC 6752 and NGC 6397 (Moehler et al. 2004), as well as in the open cluster NGC 2099 (Kalirai et al. 2005). While this has not been tested in 47 Tuc to date, we make the assumption that our sample consists of DA WDs, but we also compare our results to that obtained considering DB models and a mixture of DA and DB WDs.

WDs within globular clusters are faint objects in crowded fields, making their identification quite challenging. However, with carefully planned observations with the HST, combined with thorough data reduction and analysis, it becomes possible to obtain high quality multi-band photometry of WDs in large samples within one cluster system (see the recent observations of WDs in M4 and NGC 6397 from Richer et al. 2002; Hansen et al. 2002, 2007; Richer et al. 2008).

2. DATASET

We obtained HST images of the Galactic globular cluster 47 Tuc in cycle 17 (GO-11677, PI - H. Richer) with the Advanced Camera for Surveys (ACS) and the WFC3. The primary field of this program was imaged with the ACS/WFC in F606W and F814W filters for 121 orbits.

¹¹ To first order, we find that when examining the turn off magnitude, the age uncertainty is approximately equal to $(10 \text{ Gyr/mag}) \times (\text{uncertainty in the distance modulus})$.

Additional fields were taken with the WFC3 using both the UVIS and IR channels. Our observational design and reduction are discussed in detail in Kalirai et al. (2011), here we briefly review the WFC3 dataset used in the present analysis. With the WFC3, we obtained 121 orbits covering > 60 arcmin² and extending over 250 degrees in azimuthal range of 47 Tuc. This covers a radial range of $5 - 13.7$ arcmin ($6.5 - 17.9$ pc) within the globular cluster. For 61 orbits, we stared in one field location in the cluster (stare field) obtaining 59 orbits of IR images in F110W and F160W and 2 orbits of UVIS images in F390W and F606W. We then swept out an arc around the cluster's center (swath fields), using 5 orbits in each of our 12 additional fields obtaining F390W, F606W, F110W and F160W images (for a visualization of our observations, see Figure 4 of Kalirai et al. 2011). The observational logs of the swath and stare fields can be found in Tables 2 & 3 of Kalirai et al. (2011).

To summarize the data analysis discussed in Kalirai et al. (2011), we retrieved the WFC3 observations from the MAST archive and re-processed all data into *_flt* images using the latest calibration files. These images were then supersampled and drizzled together, paying careful attention to image registration, sky offsets, and pixel drop size. PSF-fitted photometry and astrometry was performed on the final image stacks in each filter using DAOPHOT II and ALLSTAR. The IR swath data were too undersampled (with a native FWHM = $1.1 - 1.2$ pixels) for PSF photometry however, so photometry for each star was obtained from a small aperture radius of 3.5 pixels. The catalogs from all filters, over both the UVIS and IR cameras, were merged together using high order transformations.

3. SELECTING THE SAMPLE

In the selection of our sample of WDs, our goal was not to have the largest sample possible with the dataset, but instead to have a set of WDs that cleanly lay on the white dwarf cooling sequence and are free of possible photometric contamination. Therefore, we selected our sample using multiple criteria. Initially, we isolated the WD cooling sequence in the (F390W-F606W, F606W) CMD shown in Figure 1, selecting WD candidates down to F606W = 25.5.

Our WD cooling sequence was carefully selected to avoid possible contaminants from the main sequence of the SMC in the background. From our initial list, there were 171 WD candidates that also had F110W and F160W measurements. From these 171 candidates, we selected objects that were consistent with being stellar and passed a visual inspection of the images.

To classify an object as stellar, *full width half maxima* (FWHMs) were measured in all 4 images and compared to the mean stellar FWHM in these same images. To determine the mean stellar FWHM in each image, we measured the FWHM of 20-30 stars that lay on the main sequence between F606W = $19 - 19.5$ in the (F390W-F606W, F606W) CMD. We selected the same 20-30 stars for the 4 filters in each field. We removed candidate objects from our list of 171 candidates that differed in their measured FWHM by more than 1 standard deviation from the mean stellar value in the F160W filter. We chose the F160W filter because the resolution of the images are the lowest in our sample and the WDs are thus

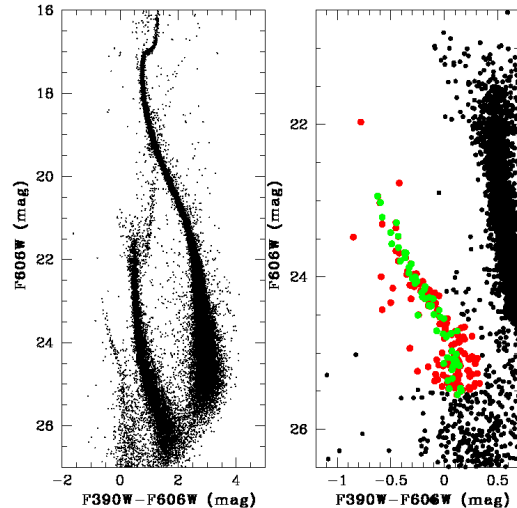


FIG. 1.— *Left:* The UVIS CMD of the objects in the stare and swath fields. The reddest sequence is the main sequence of 47 Tuc and the bluest sequence is the cluster's WD cooling sequence. The intermediate sequence is the main sequence and turn off region of the SMC in the background. *Right:* A closer examination of the 47 Tuc WD cooling sequence. Our final selection of 59 WDs are shown as green (light grey) circles while the remaining 112 candidate WDs are shown as red (dark grey) circles. A color version of this figure is available in the electronic version.

more likely to be contaminated by nearby neighbors. We are also interested in searching for IR excess in the WD photometry. This may be indicative of a debris disk or a low mass companion (see Section 6.1). While most of the IR excess, if present, will be evident at wavelengths longer than F160W, this program could be able to see hints of the excess in the F160W band which may be followed up in future observations. As such, we are particularly critical of the F160W measurements. The distributions of stellar FWHMs and the final selected WDs are shown in Figure 2.

Independent of our size rejection analysis, we also visually examined the F390W, F606W, F110W, and F160W images for the 171 WD candidates to search for objects that appeared elliptical or whose photometry may have been contaminated by bright neighboring stars, diffraction spikes, remaining cosmic rays, or those found in extremely crowded regions with varying background. If the candidate object was contaminated in any of the four filters, it was rejected from our list.

We found in these two search methods that all of our visually rejected objects were also rejected using our FWHM technique. For a few objects, we were unable to measure a reliable FWHM in F160W, so we accepted these objects into our final list if their FWHMs were stellar in the three additional bands and they did not appear contaminated on the images. Our final selection consists of 59 WDs listed in Table 2 with their field location, R.A. and Decl. (in J2000 epoch), their F390W, F606W, F110W, and F160W photometric measurements and uncertainties in VEGAMAGS, and the effective temperatures that we fit in this study. In Figure 3, we show the F390W, F606W, F110W, and F160W images for our sample WDs. Two of these WDs were found near the edge of their F390W and F606W images. For these two

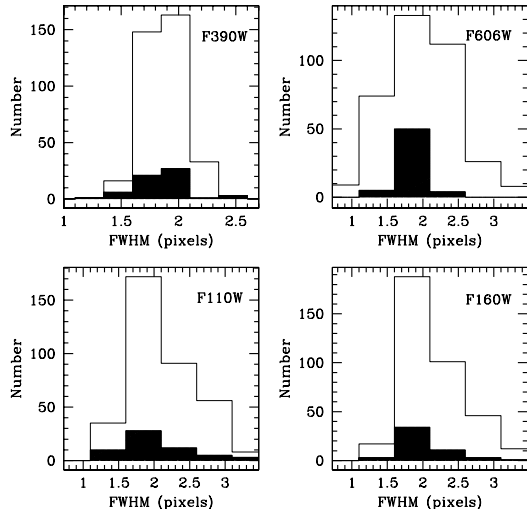


FIG. 2.— The measured FWHMs for main sequence stars between $F606W = 19 - 19.5$ magnitudes in all fields are shown as the open histogram for the filters (*top left*) F390W, (*top right*) F606W, (*bottom left*) F110W, and (*bottom right*) F160W. The solid histograms are the measured FWHMs for the 59 selected WDs.

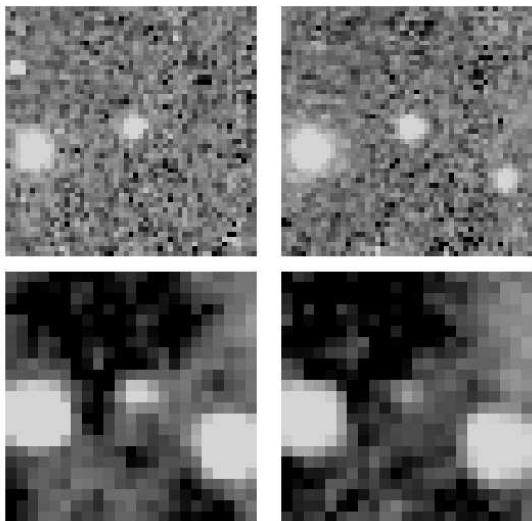


FIG. 3.— A four panel image of WD 1. Within the four panels, the *upper left* is F390W, *upper right* is F606W, *lower left* is F110W, and *lower right* is F160W. The WD is centered in the $2'' \times 2''$ images and its photometry is listed in Table 2.

filters, there were only two exposures combined to produce the final image and thus some cosmic rays were not removed due to the offset between the two exposures. This is evident in Fig. 3 for WDs 23 and 52 but does not affect our photometry in these bands obtained with PSF fitting.

4. SPECTRAL ENERGY DISTRIBUTIONS

4.1. Model Conversion to our Photometric System

In order to generate the spectral energy distributions of WDs in 47 Tuc, we have chosen to use the Tremblay et al. (2011) spectral model grids of pure hydrogen atmosphere WDs. These model grids define spectra for objects with surface gravities ($\log(g)$) ranging from 6 – 10 in steps of 0.5 and effective temperatures (T_{eff}) from

6000 – 120000 K. The spectral grid is defined in steps of 500 K between 6000 – 17000 K, steps of 5000 K between 20000 – 90000 K, and steps of 10000 K between 90000 – 120000 K. We have converted the model grids to our observed Space Telescope magnitudes (STMAG), similar to the procedure of Bergeron et al. (1997), to obtain a magnitude for each of our observed filters, M_{STMAG} . This enables us to fit the models to our observations via Equation 1,

$$M_{\text{STMAG}} = -2.5 \log_{10} \left(\frac{\frac{R^2}{d^2} \int_0^\infty \lambda F_{\text{mod}} E_\lambda S_\lambda d\lambda}{\int_0^\infty \lambda F_0 S_\lambda d\lambda} \right) \quad (1)$$

where F_{mod} is the flux per unit wavelength for the spectral model integrated over the solid angle, S_λ is the total system throughput for the filter¹², and E_λ is the standard interstellar extinction curve (Fitzpatrick 1999) with $A_V / E(B - V) = 3.1$, using some input $E(B - V)$. The STMAG zeropoints are defined so that a flat spectrum of $3.63 \times 10^{-9} \text{ ergs cm}^{-2} \text{ s}^{-1} \text{ \AA}^{-1}$ (F_0) through any filter yields a magnitude of zero.

The inclusion of the λ terms in Equation 1 is required because of how the flux is measured on a CCD. The CCD does not know the individual energy of each photon that it receives, only whether or not it has received a photon. For any given energy density, the number of photons received will increase linearly with wavelength. For a relatively flat spectrum, fluxes measured on a CCD through some filter will therefore be more affected by the energy flux at longer wavelengths. This is because this region of the spectrum will necessarily have a higher number of photons per unit energy as the energy of a photon is inversely proportional to its wavelength ($E_{\text{photon}} = ch/\lambda$).

The factor of $(R/d)^2$ in Equation 1 scales the model flux, the flux per unit wavelength at the surface of the object, to the observed flux for a star of radius R , at a distance d . Equation 1 can then be rewritten as,

$$M_{\text{STMAG}} = -2.5 \log_{10} \left(\frac{\int_0^\infty \lambda F_{\text{mod}} E_\lambda S_\lambda d\lambda}{\int_0^\infty \lambda F_0 S_\lambda d\lambda} \right) + 5 \log_{10} \left(\frac{d}{R} \right) \quad (2)$$

Equation 2, which is illustrated in Figure 4, shows that the model magnitude in any given filter is a function of only $\log(g)$, T_{eff} , reddening, and d/R . We apply this method to convert the model grid magnitudes to our four filters (F390W, F606W, F110W, and F160W).

4.2. Fitting the Model SEDs to the WD Photometry

Using WD cooling models from Fontaine et al. (2001), we can derive a relationship between surface gravity and effective temperature for a given mass (see Figure 5). Additionally, for any given mass and $\log(g)$, we can calculate the radius from Equation 3.

$$R = \sqrt{\frac{GM}{g}}. \quad (3)$$

¹² The STMAG zeropoints and throughput values for each filter have been obtained from the *Space Telescope Science Institute* website (http://www.stsci.edu/hst/wfc3/phot_zp_lbn, http://www.stsci.edu/hst/wfc3/ins_performance/throughputs).

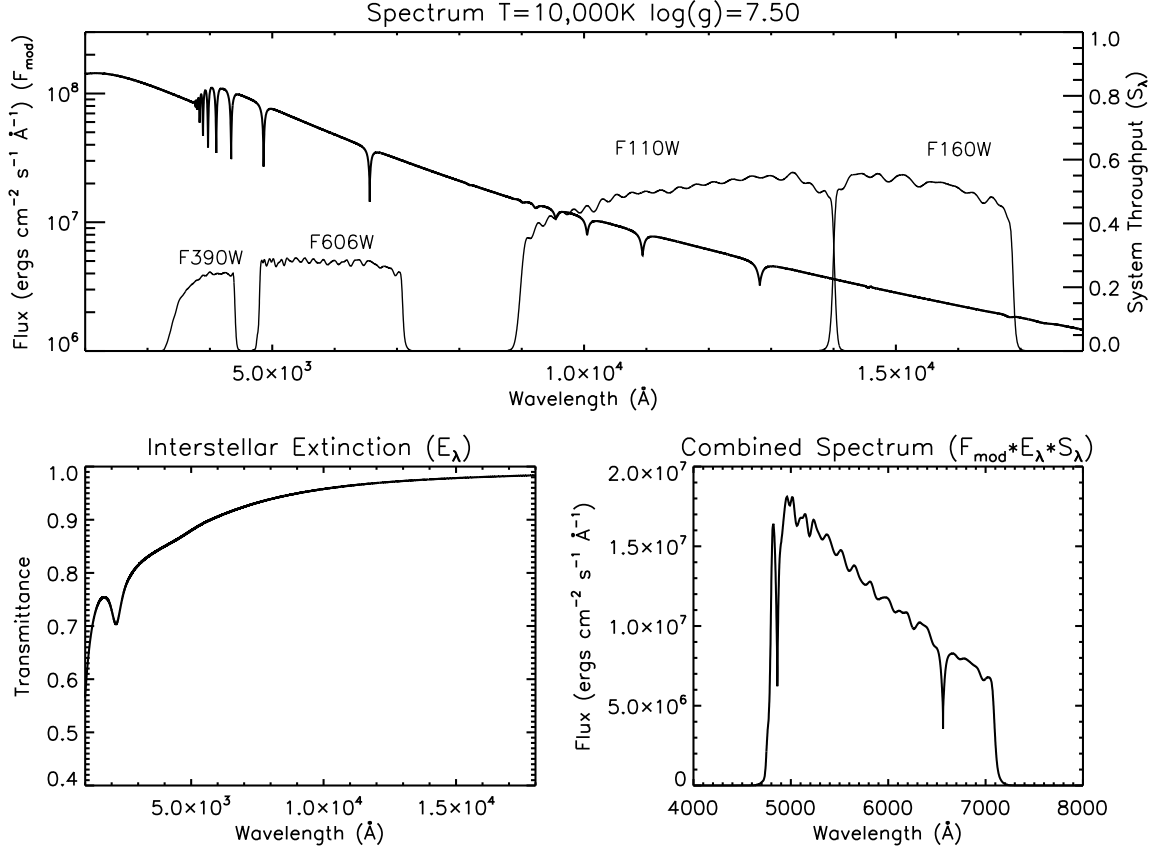


FIG. 4.— An illustration of Equation 2 for a sample model spectrum converted to an F606W magnitude. *Upper panel:* An example model spectrum from Tremblay et al. (2011) (F_{mod}) for a DA WD with an effective temperature of 10 000 K and surface gravity of 7.50. Overlaid are the four filter throughputs S_{λ} (F390W, F606W, F110W, and F160W). *Lower left:* The interstellar extinction. *Lower right:* The combined spectrum.

Putting the mass dependent T_{eff} - $\log(g)$ relation together with Equation 3 means that, of the four parameters, T_{eff} , $\log(g)$, mass, and radius, the combination of T_{eff} and any of the other three allows one to calculate the remaining two parameters. Of these four, we have chosen to parametrize our grid over T_{eff} and mass, since previous work allows us to put a reasonable prior on the mass of our objects. This reduces the six parameters that control each WD spectrum (effective temperature, mass, distance, reddening, surface gravity, and the radius of the WD) to four parameters that need to be fit in our procedure. We are therefore able to generate a model SED in these four filters given a mass, effective temperature, reddening, and a distance. The first three parameters control the shape of the SED, while the distance controls the overall scaling. In order to determine temperatures for our WDs and to display both model and WD SEDs, we have first held mass and reddening as constants in our fitting procedure. We have assumed a mass of $0.53 M_{\odot}$. This follows from the prediction of Renzini & Fusi Pecci (1988) and Renzini et al. (1996) that the WDs forming today in globular clusters should have a mass of $0.53 \pm 0.02 M_{\odot}$. Further support of our mass selection comes from recent direct spectroscopic measurements from Kalirai et al. (2009) of $0.53 \pm 0.01 M_{\odot}$ for the mass of WDs in M4 and $0.53 \pm 0.03 M_{\odot}$ for the mass of WDs in NGC 6752 (Moehler et al. 2004).

We also assume a reddening of 0.04 and then fit the dis-

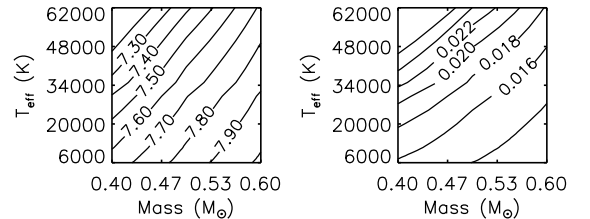


FIG. 5.— *Left:* Contours of constant surface gravity ($\log(g)$) in mass-effective temperature (T_{eff}) space and *Right:* Contours of constant radius, measured in units of solar radii, in mass- T_{eff} space from Tremblay et al. (2011).

tance modulus and the effective temperature to each individual object. We ignore the individual distance moduli here and include the fitted effective temperatures in Table 2 for our 59 WDs. Figure 6 shows the SEDs for our selected WD sample.

In Section 5, we determine the distance to 47 Tuc using Equation 2 to fit to our WD photometry, however we do so using a maximum likelihood function and marginalise over various parameters.

5. DISTANCE TO 47 TUC

To determine the distance to 47 Tuc, we will use white dwarf spectral models in order to predict an expected absolute magnitude for our sample WDs in our 4 filters, similarly to our technique in Section 4. However in this section, we fit the distance modulus to 47 Tuc by com-

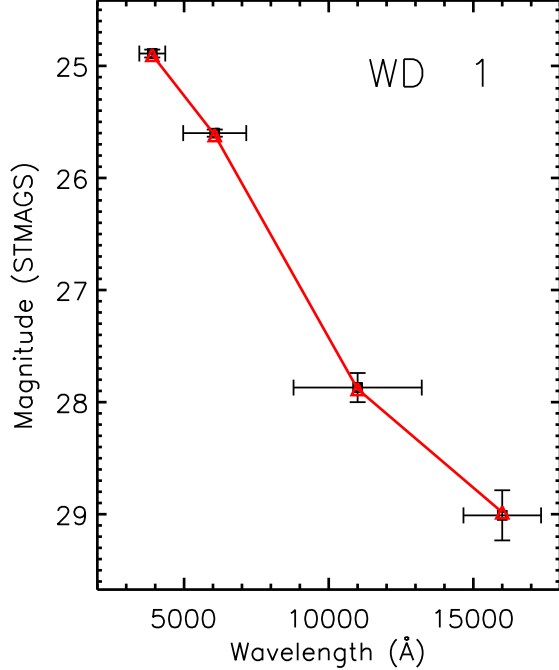


FIG. 6.— The SED for WD 1. The filled squares are our photometric measurements in F390W, F606W, F110W, and F160W with uncertainties. The wavelength range for each filter is also shown as the equivalent width of the filter divided by the maximum throughput, as defined by the WFC3 instrument handbook. The red triangles, connected by the red line is the best fit model in STMAG magnitudes. A color version of this figure is available in the electronic version.

paring the expected absolute magnitude to the measured apparent magnitudes of the WDs using a maximum likelihood analysis that uses all 59 WDs to determine one final distance to the cluster. Unlike in Section 4, we do not assume a single value for reddening and WD mass in the determination below, rather we marginalise over each of these parameters with the inclusion of Gaussian priors.

5.1. Maximum Likelihood Function

Our procedure begins by calculating the likelihood function of our 59 WDs, termed L_j where j runs from 1–59, over our four parameters of T_{eff} , reddening, mass, and distance which is simply converted to a true distance modulus, $(m - M)_0$. This is shown in Equation 4

$$L_j(\text{data} | (T_{\text{eff}}, (m - M)_0, \text{mass}, E(B - V))) = \quad (4)$$

$$\prod_{i=1}^4 \exp \left[-\frac{(\text{data}_i - \text{mod}_i)^2}{2\sigma_i^2} \right].$$

The photometric data for each WD (termed data_i) are the measured magnitudes in our 4 filters, mod_i are the magnitudes calculated from the model described in Equation 2 from Section 4, and σ_i are the uncertainties for each point.

After a likelihood for each white dwarf is calculated using Equation 4, we use Bayes' Theorem as well as a Gaussian prior on the mass with a mean of $0.53 M_\odot$ and a standard deviation of $0.02 M_\odot$, and a uniform prior on

the temperature, to calculate the likelihood of the model parameters $(m - M)_0$ and $E(B - V)$ for each individual object, given the data. This step is described in Equation 5

$$L_j(((m - M)_0, E(B - V)) | \text{data}) \propto (5)$$

$$\int_0^\infty \int_0^\infty L_j(\text{data} | (T_{\text{eff}}, (m - M)_0, \text{mass}, E(B - V)))$$

$$\times \exp \left[-\frac{(0.53 - \text{mass})^2}{2(0.02)^2} \right] d\text{mass} dT_{\text{eff}}.$$

We then combine the distance modulus-reddening likelihood of all 59 WDs described in Equation 6

$$L(((m - M)_0, E(B - V)) | \text{data}) = \quad (6)$$

$$\prod_{j=1}^{59} L_j(((m - M)_0, E(B - V)) | \text{data})$$

and marginalise over the reddening parameter with a Gaussian prior with a mean of 0.04 and a $\sigma = 0.02$. From this, we obtain the distribution function for the cluster as a whole, described in Equation 7 and shown in Figure 7.

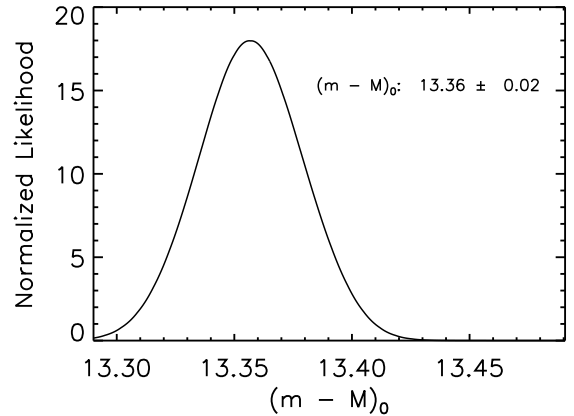


FIG. 7.— The combined distribution function of distance modulus for the sample of 59 WDs. The peak of the distribution at 13.36 is the unreddened distance modulus value we quote for 47 Tuc along with its statistical uncertainty of 0.02.

Our best fit unreddened distance modulus using these priors on mass and reddening is 13.36 ± 0.02 .

$$L(((m - M)_0) | \text{data}) = \quad (7)$$

$$\int_0^\infty L((m - M)_0, E(B - V)) | \text{data})$$

$$\times \exp \left[-\frac{(0.04 - E(B - V))^2}{2(0.02)^2} \right] dE(B - V)$$

Additionally, we consider how our distance estimate depends on our assumptions about the mass and reddening. To do this, we can consider our original four parameter likelihood grid for each of our 59 white dwarfs. After marginalising out the effective temperature for each WD individually and combining the likelihood of all 59 WDs in Eqn. 6, we are left with the likelihood values on a grid over reddening, mass, and distance modulus. For each combination of reddening and mass on the grid, there is

a corresponding one-dimensional distance modulus likelihood distribution. The most likely distance modulus can then be found for each mass and reddening pair. The result is a surface of most likely distance modulus values that is well approximated by a plane, described as

$$(m - M)_o = 14.634 - (2.573 * \text{mass}) + (2.552 * E(B - V)) \quad (8)$$

where the mass is in solar masses. This approximation to our likelihood grid is accurate to 0.003 mag and is valid only within the ranges of mass ($0.50 - 0.56 M_\odot$) and reddening ($0 - 0.08$).

5.2. Fitting the SEDs with DB Atmosphere Models

Here we test the assumption that the WDs in our sample are DA atmosphere WDs by fitting our sample of 59 WDs instead with DB atmosphere models (Bergeron et al. 2011). The SEDs fit with the DB models return temperatures that are on average 2200 K cooler than the fits with the DA models. These cooler temperatures result in objects that are fainter and thus our true distance modulus is closer to a value of 12.90. If we compare the likelihoods of these fits, 53 of our 59 WDs have a higher likelihood value for our best fit DA model, with 48 being better by a factor of 10 or more and 22 being better by a factor of 10^4 or more. The 6 remaining WDs that were fit better by a DB model have an average likelihood that is better by a factor of 2. Additionally, the standard deviation of the differences between the best fit model and all 59 WDs is 0.11 mag for the DA models and 0.18 mag for the DB models.

In the field population of WDs, Tremblay & Bergeron (2008) found the ratio of DB to DA to be approximately 25% in the temperature range of our WD sample. We test the effect on the determined distance modulus if 25% of our sample were instead DB WDs, by randomly fitting 25% of our WDs by DB models and the rest with DA models. Under these conditions, the distance modulus is 13.32 with a random uncertainty of 0.06, easily encompassing our distance modulus assuming all DA WDs.

5.3. Error Analysis

The statistical error of 0.02 that is quoted from our maximum likelihood analysis in Section 5.1 are 1σ upper and lower errors for the distance modulus calculated directly from the summed likelihood distribution in Fig. 7. The systematic errors were determined entirely from the uncertainties in our photometric calibration taken from Kalirai et al. (2011). We generate 10 synthetic WD SEDs from the models of Tremblay et al. (2011) evenly spaced between 8000 – 32000 K, spanning the range of effective temperature of our WD sample. We performed the same likelihood analysis as in Section 5.1 using the uncertainties in the photometric calibration as the errors on each magnitude. For each of the 10 WDs, we extract a distance modulus from their likelihood distributions along with the width of the distribution as the error. The widths of the likelihood distributions must be due solely to our photometric calibration uncertainties, as these synthetic objects come directly from the model grids. Figure 8 shows the systematic errors as a function of effective temperature for the synthetic WDs fit with a cubic spline function. For each of our 59 WDs, we used

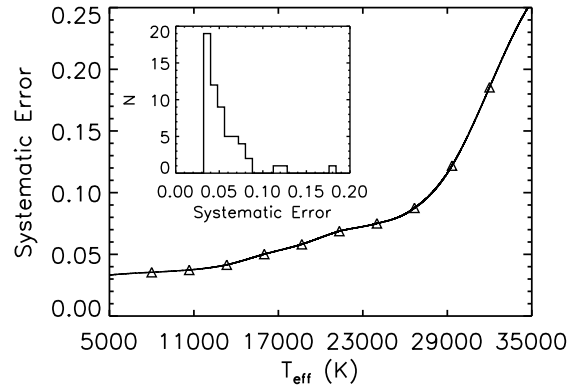


FIG. 8.— The systematic uncertainties of the distance modulus as a function of effective temperature (T_{eff}) for 10 synthetic WDs (triangles) fit with a cubic spline function. *Inset:* The distribution of systematic errors for the 59 WDs in our sample determined from the spline fit. Our quoted systematic uncertainty for the distance modulus of 47 Tuc is the mean of the sample of 59 WDs.

the effective temperature to obtain the systematic error on its determined distance modulus from the spline fit in Fig. 8. For the final calibration error on the distance modulus of 47 Tuc, we quote the mean systematic error of the 59 WDs.

Using this technique, we have determined the true distance modulus to 47 Tuc to be $13.36 \pm 0.02(\text{random}) \pm 0.06(\text{systematic})$ corresponding to a distance of $4.70 \pm 0.04(\text{random}) \pm 0.13(\text{systematic})$ kpc. An unknown fraction of DB objects in our sample will systematically change this result, giving us a smaller distance modulus, and wider error bars as the fraction increases. The closer distance results from the fact that DB white dwarfs of roughly the same SED shape are brighter than DAs, meaning we would have to fit them closer in order to match the observed magnitudes. The wider error bars result from the fact that DB models almost universally fit our objects worse than DA models. Additionally, we don't know which objects are DBs, and so this causes a systematic error that needs to be addressed by iterating our fitting routine while randomly assigning some fraction of our objects to be fit as DBs rather than DAs each time. The fit distance modulus and errors both change roughly linearly with DB fraction, as shown in Figure 9. At 0% DBs we have the quoted fit values, at 25% DBs we have $13.32 \pm 0.06 \pm 0.06$.

We have tried a number of variations in order to assess how the distance modulus changes by varying some of our input assumptions. The white dwarfs forming in globular clusters today should have masses between $0.51 - 0.55 M_\odot$ (Renzini & Fusi Pecci 1988; Renzini et al. 1996). As discussed in Section 5.1, we have used a Gaussian prior on the mass with a mean of $0.53 M_\odot$ and a $\sigma = 0.02$ in our distance determination. Based on Eqn 8, if we instead assume a WD mass of $0.50 M_\odot$ and $0.56 M_\odot$, our unreddened distance moduli becomes 13.45 and 13.30, respectively. The reddening towards 47 Tuc has estimates ranging between $E(B - V) = 0.024$ (Gratton et al. 2003) and $E(B - V) = 0.055$ (Gratton et al. 1997) in the literature. If we fix the reddening values to $E(B - V) = 0.024$ and $E(B - V) = 0.055$, we obtain unreddened distance moduli of 13.33 and 13.41, respectively. Despite various changes to our initial assumptions, these are all consistent with our distance modulus of 13.36 given the random

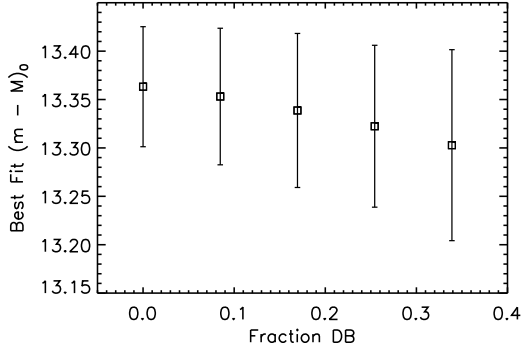


FIG. 9.— The best fit distance modulus shown with varying fractions of DB/DA WDs in our sample. The uncertainties shown are the random and systemic uncertainties added in quadrature.

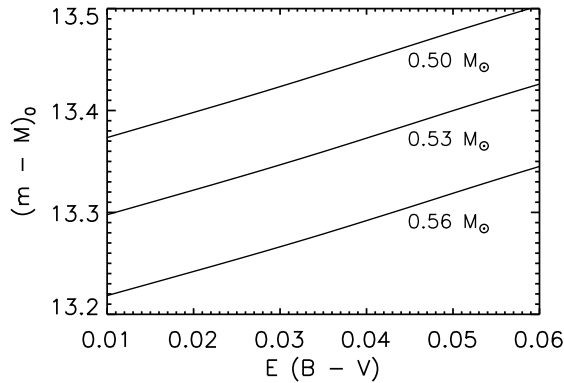


FIG. 10.— The distance modulus determined from our maximum likelihood technique shown as a function of reddening for various slices in WD mass space.

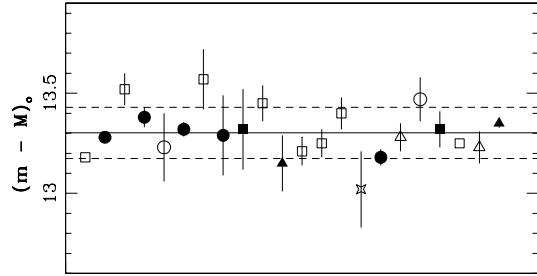


FIG. 11.— The previously determined unreddened distance moduli of 47 Tuc including the value from this study, plotted with their statistical uncertainties. The distances plotted from right to left are listed in Table 1 from top to bottom. Our new measurement is the final point on the right. The different symbols represent the various methods used in the distance determination: main sequence fitting (*open squares*), horizontal branch fitting (*filled circles*), RR Lyrae (*open circles*), tip of the red giant branch (*closed squares*), methods using the white dwarfs (*filled triangle*), cluster kinematics (*cross*), and eclipsing binaries (*open triangles*). The *solid line* is the mean of the 22 distance moduli measurements ($\langle (m - M)_0 \rangle = 13.30$) and the *dashed lines* are one standard deviation ($\sigma = 0.13$).

uncertainties of 0.02 on each distance and the systematic uncertainty of 0.06 quoted above. We show in Figure 10 how the distance modulus changes as a function of reddening taken at different WD masses, all spanning the ranges in the literature. Again, we find all reasonable assumptions of the initial parameters to be consistent within our quoted uncertainties.

As a summary, we show the previous distance determinations to 47 Tuc in Table 1 including the distance determined here in Figure 11. These values have been dereddened, where appropriate, using $E(B - V) = 0.04$ and $A_V / E(B - V) = 3.1$. We find the mean of these measurements to be $\langle (m - M)_0 \rangle = 13.30$ with a standard error of the mean of 0.03 and a standard deviation of 0.13.

6. DISCUSSION

6.1. A Search for Infrared Excess

Our dataset also provides us the opportunity to search for evidence of extrasolar planetary systems. A previous search for planets in the core of 47 Tuc was performed by Gilliland et al. (2000) using a time-series analysis over 8.3 days searching for close in Jupiter-sized planets around ~ 34000 main sequence stars. They concluded that no light curve in their sample strongly suggested the presence of a planet, indicating that the planet frequency in 47 Tuc may be an order of magnitude less than in our solar neighborhood. This may be expected in the dense stellar environment of the core of 47 Tuc which could lead to orbit disruption and/or hinder planet survival. In addition, the planet-metallicity correlation indicates that the frequency of planets increases with the host star's metallicity (e.g. Fischer & Valenti 2005), making it even less likely to find a planet around a star with subsolar metallicities in 47 Tuc.

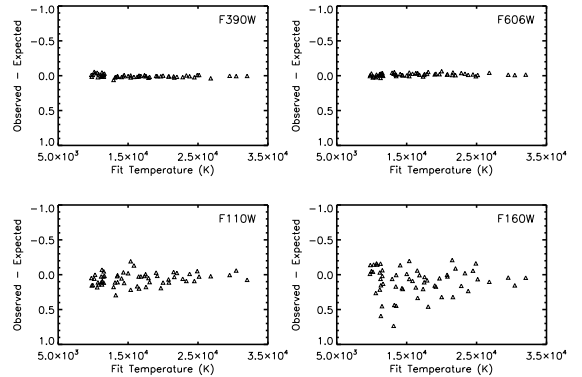


FIG. 12.— The observed minus the expected model magnitudes as a function of effective temperature (T_{eff}) for our WD sample in the four filters F390W (*upper left*), F606W (*upper right*), F110W (*lower left*), and F160W (*lower right*).

Our dataset enables us to instead search for evidence of extrasolar planetary systems with the SEDs of our selected WDs. WDs have essentially metal-free atmospheres (Paquette et al. 1986; Zuckerman et al. 2003) and low luminosities, allowing for the detection of cool low mass counterparts, such as debris or circumstellar disks, as well as planets or brown dwarfs (Probst 1983; Zuckerman & Becklin 1987a; Farihi et al. 2005; Burleigh et al. 2006). One form of evidence for the existence of these features is the presence of IR excess (Zuckerman & Becklin 1987b; Graham et al. 1990; Kilic et al. 2006; von Hippel et al. 2007; Farihi et al. 2008, among others). The likelihood of a WD having an IR excess is correlated with its T_{eff} and/or presence of photospheric metals (Farihi et al. 2009), the most well studied of which is calcium. The pollution of hydrogen-

rich photospheres of WDs with metals could be caused by circumstellar accretion. If a planetesimal or asteroid is tidally disrupted, a circumstellar dust disk could arise (Jura 2003, 2008) and likely pollute the WD's atmosphere with detectable metals.

With no prior information about the calcium abundance of the WDs in our study, we examine their T_{eff} . Of our 59 WDs, all but 3 have fitted $T_{\text{eff}} > 10000$ K, with the remaining three having $T_{\text{eff}} = 9684 \pm 1041$ K, $T_{\text{eff}} = 9804 \pm 921$ K, and 9924 ± 841 K. We can estimate how many cases of IR excess we expect to see in our sample using upper and lower bounds provided by various studies in the literature. Recent work by Zuckerman et al. (2010) show that $\sim 30\%$ of the photospheres of white dwarfs with T_{eff} between 13500–19500 K show evidence for being polluted with metals. In the same temperature range, approximately 20% of DA WDs with metal bearing photospheres also show evidence for warm circumstellar material (Kilic et al. 2008). This indicates a fraction of dusty WDs to be 6%, which we take as an upper limit. A lower limit to the fraction of warm DA WDs with dusty disks is $\sim 1\%$ (Farihi et al. 2009), obtained from recent large WD surveys (Liebert et al. 2005; Koester et al. 2005; Farihi et al. 2005; Hoard et al. 2007; McCook & Sion 1999). From our 171 (59) WDs, we therefore expect between $\sim 2 - 10$ ($\sim 0 - 4$) WDs to have IR excess. However, our reddest photometric measurement is F160W, a wide-H band filter with a central wavelength of 1536.9 nm. This is just where the spectral energy distribution of a typical warm WD would begin to show evidence for an IR excess given a companion or disk with $T_{\text{eff}} \sim 800$ K. In addition, we must also consider our photometric uncertainties. It thus seems unlikely that we would find clear evidence for an IR excess in our best sample of WDs. However, if we do find indication for IR-excess in the H band, it could be confirmed with additional observations in redder filters.

We have searched the SEDs in Figure 6 of all our WD candidates for evidence of an IR excess, focusing on the examination of the F160W band. Any evidence that we found for an enhanced F160W measurement appeared to be due to contamination by neighboring stars, diffraction spikes, or cosmic rays. In addition, for each filter, we plot the observed magnitude minus the expected model magnitude as a function of effective temperature for each of our 59 WDs, shown in Figure 12. The few outlying points in the F160W filter at lower temperature are objects that are too faint compared to the models, driven by large photometric uncertainties. If IR excess is present, we would expect to see points with negative values on the y-axis. Figure 12 indicates that in the F160W band, our WDs are at most in excess of 0.2 magnitudes compared to the model. We question whether this could indicate a cool brown dwarf companion or debris disk. Using the evolutionary models for cool brown dwarfs and exosolar giant planets of Baraffe et al. (2003), we combine a typical WD in our sample with the contribution from a 10 Gyr dust free cool brown dwarf. Here, we convert the model IR data from the CIT system to that of 2MASS using the transformations of Carpenter (2001), as 2MASS is a nearly identical photometric system to that in WFC3 and provides the closest comparison possible. In Figure 13, we show that for masses of a companion below $0.06 M_{\odot}$ ($\sim 60 M_J$), we would be unable to detect it.

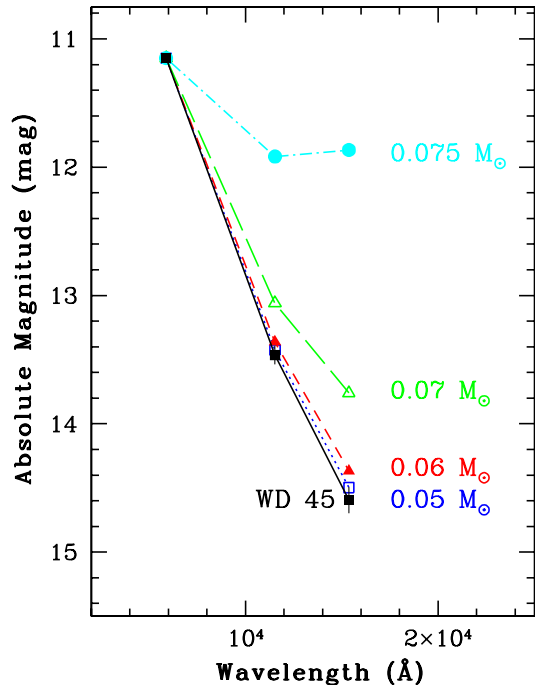


FIG. 13.— The observed F606W, F110W, and F160W magnitudes for a typical WD in our sample (*solid squares*). Also shown are the added contribution to these magnitudes from a 10 Gyr dust free cool brown dwarf companion with masses of $0.05 M_{\odot}$ ($\sim 50 M_J$) as *open blue squares*, $0.06 M_{\odot}$ ($\sim 60 M_J$) as *solid red triangles*, $0.07 M_{\odot}$ ($\sim 70 M_J$) as *open green triangles*, and $0.075 M_{\odot}$ ($\sim 75 M_J$) as *solid cyan circles* from the Baraffe et al. (2003) models. Here, we have converted the model magnitudes to that of 2MASS using the transformations in Carpenter (2001). In order for us to detect a cool brown dwarf companion from our sample, the companion must be at least $0.06 M_{\odot}$, which is an excess of 0.23 magnitudes in the F160W filter. A color version of this figure is available in the electronic version.

However, a cool brown dwarf with $0.06 M_{\odot}$, may be detectable, as this leads to a difference in magnitude in the F160W band of > 0.23 magnitudes. Examining Figure 12, it is clear that none of our 59 WDs have F160W in excess of 0.2 from the models. We conclude that we do not find any case in our sample that shows strong evidence for a genuine IR excess. Our search for planets in 47 Tuc continues, however, with this cycle 17 dataset. We have time series data of two fields outside the core of 47 Tuc, one is the stare field described in Section 2 consisting of F110W and F160W observations over ~ 20 days with 10000 stars, and the other field has ACS images in F606W and F814W filters spanning ~ 9 months with 20000 stars. Our analysis, currently underway, will be able to put a constraint on the binary frequency within 47 Tuc and search for exoplanets by analysis of the stellar light curves (Woodley et al. 2012). Not only will we examine the light curve of main sequence stars down to $\sim 0.2 M_{\odot}$, but we will also be able to search for planets around the brighter WD population. A small radius ratio between the WDs and giant gas planets will significantly aid in our planetary search.

6.2. Summary

With this new HST dataset of the Galactic globular cluster 47 Tuc, we have examined the SEDs of a sample of 59 WDs that are devoid of pho-

tometric contamination by neighboring stars or image defects. From this sample of SEDs, we have applied a novel approach to simultaneously estimate the distance of 47 Tuc from the comparison of theoretical model WD atmospheres (Tremblay et al. 2011). We obtain a true distance modulus of $13.36 \pm 0.02(\text{random}) \pm 0.06(\text{systematic})$ corresponding to a distance of $4.70 \pm 0.04(\text{random}) \pm 0.13(\text{systematic})$ kpc.

We thank our referee who provided a very careful,

comprehensive, and thoughtful report. We extend our thanks to Dr. Zoccali for providing us with local white dwarf photometry. Support for the program GO-11677 was provided by NASA through a grant from the Space Telescope Science Institute, which is operated by the Association of Universities for Research in Astronomy, Inc., under NASA contract NAS 5-26555. This work is supported in part by the NSERC Canada and by the Fund FQRNT (Québec)

REFERENCES

- Baraffe, I., Chabier, G., Barman, T. S., Allard, F., & Hauschildt, P. H. 2003, *A&A*, 402, 701
- Becklin, E. E., Farihi, J., Jura, M., Song, I., Weinberger, A. J., & Zuckerman, B. 2003, *ApJ*, 632, L119
- Bergeron, P., Ruiz, M. T., & Leggett, S. K. 1997, *ApJS*, 108, 339
- Bergeron, P., Wesemael, F., Dufour, P., Beauchamp, A., Hunter, C., Saffer, R. A., Gianninas, A., Ruiz, M. T., Limoges, M.-M., Dufour, P., Fontaine, G., & Liebert, J. 2011, *ApJ*, 737, 28
- Bergbusch, P. A. & Stetson, P. B. 2009, *AJ*, 138, 1455
- Bolte, M. & Hogan, C. 1995, *Nature*, 376, 399
- Bono, G., Stetson, P. B., Sanna, N., Piersimoni, A., Freyhammer, L. M., Bouzid, Y., Buonanno, R., Calamida, A., Caputo, F., Corsi, C. E., Di Cecco, A., Dall'Ora, M., Ferraro, I., Iannicola, G., Monelli, M., Nonino, M., Pulone, L., Sterken, C., Storm, J., Tuvikene, T., & Walker, A. R. 2008, *ApJ*, 686, L87
- Brown, T. M., Sahu, K., Zoccali, M., Renzini, A., Ferguson, H. C., Anderson, J., Smith, E., Bond, H. E., Minniti, D., Valenti, J. A., Casertano, S., Livio, M., Panagia, N., Vanden Berg, D. A., & Valenti, E. 2009, *AJ*, 137, 3172
- Burleigh, M. R., Hogan, E., Dobbie, P. D., Napiwotzki, R., & Maxted, P. F. L. 2006, *MNRAS*, 373, L55
- Carpenter, J. M. 2001, *AJ*, 121, 2851
- Carretta, E., Gratton, R. G., Clementini, G., & Fusi Pecci, F. 2000, *ApJ*, 533, 215
- Carretta, E., Bragaglia, A., Gratton, R., D'Orazi, V., & Lucatello, S. 2009, *A&A*, 508, 695
- Cassisi, S. & Salaris, M. 1997, *MNRAS*, 285, 593
- Davis, D. S., Richer, H. B., Rich, R. M., Reitzel, D. R., & Kalirai, J. S. 2009, *ApJ*, 705, 398
- Di Cecco, A., Bono, G., Stetson, P. B., Pietrinferni, A., Becucci, R., Cassisi, S., Degl'Innocenti, S., Iannicola, G., Prada Moroni, P. G., Buonanno, R., Calamida, A., Caputo, F., Castellani, M., Corsi, C. E., Ferraro, I., Dall'Ora, M., Monelli, M., Nonino, M., Piersimoni, A. M., Pulone, L., Romaniello, M., Salaris, M., Walker, A. R., & Zoccali, M. 2010, *ApJ*, 712, 527
- Dotter, A., Sarajedini, A., Anderson, J., Aparicio, A., Bedin, L. R., Chaboyer, B., Majewski, S., Marín-Franch, A., Milone, A., Paust, N., Piotto, G., Reid, I. N., Rosenberg, A., & Siegel, M. 2010, *ApJ*, 708, 698
- Farihi, J., Becklin, E. E., & Zuckerman, B. 2005, *ApJS*, 161, 394
- Farihi, J., Zuckerman, B., & Becklin, E. E. 2008, 674, 431
- Farihi, J., Jura, M., & Zuckerman, B. 2009, *ApJ*, 694, 805
- Ferraro, F. R., Messineo, M., Fusi Pecci, F., de Palo, M. A., Straniero, O., Chieffi, A., & Limongi, M. 1999, *AJ*, 118, 1738
- Ferraro, F. R., Montegriffo, P., Origlia, L., & Fusi Pecci, F. 2000, *AJ*, 119, 1282
- Fischer, D. A. & Valenti, J. 2005, *ApJ*, 622, 1102
- Fitzpatrick, E. L. 1999, *PASP*, 111, 63
- Fontaine, G., Brassard, P., & Bergeron, P. 2001, *PASP*, 113, 409
- Freedman, W. L., Madore, B. F., Gibson, B. K., Ferrarese, L., Kelson, D. D., Sakai, S., Mould, J. R., Kennicutt, Jr., R. C., Ford, H. C., Graham, J. A., Huchra, J. P., Hughes, S. M. G., Illingworth, G. D., Macri, L. M., & Stetson, P. B. 2001, *ApJ*, 553, 47
- Gilliland, R. L., Brown, T. M., Guhathakurta, P., Sarajedini, A., Milone, E. F., Albrow, M. D., Baliber, N. R., Bruntt, H., Burrows, A., Charbonneau, D., Choi, P., Cochran, W. D., Edmonds, P. D., Frandsen, S., Howell, J. H., Lin, D. N. C., Marcy, G. W., Mayor, M., Naef, D., Sigurdsson, S., Stagg, C. R., Vandenberg, D. A., Vogt, S. S., & Williams, M. D. 2000, *ApJ*, 545, L47
- Graham, J. R., Matthews, K., Neugebauer, G., & Soifer, B. T. 1990, *ApJ*, 357, 216
- Goldsbury, R., Richer, H. B., Anderson, J., Dotter, A., Sarajedini, A., & Woodley, K. 2010, *AJ*, 140, 1830
- Gratton, R. G., Bragaglia, A., Carretta, E., Clementini, G., Desidera, S., Grundahl, F., & Lucatello, S. 2003, *A&A*, 408, 529
- Gratton, R. G., Fusi Pecci, F., Carretta, E., Clementini, G., Corsi, C. E., & Lattanzi, M. 1997, *ApJ*, 491, 749
- Grundahl, F., Stetson, P. B., & Andersen, M. I. 2002, *A&A*, 395, 481
- Hansen, B. M. S., Brewer, J., Fahlman, G. G., Gibson, B. K., Ibata, R., Limongi, M., Rich, R. M., Richer, H. B., Shara, M. M., & Stetson, P. B. 2002, *ApJ*, 574, L155
- Hansen, B. M. S., Richer, H. B., Fahlman, G. G., Stetson, P. B., Brewer, J., Currie, T., Gibson, B. K., Ibata, R., Rich, R. M., & Shara, M. M. 2004, *ApJS*, 155, 551
- Hansen, B. M. S., Anderson, J., Brewer, J., Dotter, A., Fahlman, G. G., Hurley, J., Kalirai, J., King, I., Reitzel, D., Richer, H. B., Rich, R. M., Shara, M. M., & Stetson, P. B. 2007, *ApJ*, 671, 380
- Harris, W. E. 2010, arXiv1012.3224
- Hesser, J. E., Harris, W. E., Vandenberg, D. A., Allwright, J. W. B., Shott, P., & Stetson, P. B. 1987, *PASP*, 99, 739
- Hoard, D. W., Wachter, S., Sturch, L. K., Widhalm, A. M., Weiler, K. P., Pretorius, M. L., Wellhouse, J. W., & Gibiansky, M. 2007, *AJ*, 134, 26
- Jura, M. 2003, *ApJ*, 584, L91
- Jura, M. 2008, *AJ*, 135, 1785
- Kalirai, J. S., Richer, H. B., Hansen, B. M. S., Reitzel, D., & Rich, R. M. 2005, *ApJ*, 618, L129
- Kalirai, J. S., Davis, D. S., Richer, H. B., Bergeron, P., Catelan, M., Hansen, B. M. S., & Rich, R. M. 2009, *ApJ*, 705, 408
- Kalirai, J. S., Richer, H. B., Anderson, J., Dotter, A., Fahlman, G. G., Hansen, B. M. S., Hurley, J., King, I. R., Reitzel, D., Rich, R. M., Shara, M. M., Stetson, P. B., Woodley, K. 2011, in preparation.
- Kaluzny, J., Thompson, I. B., Rucinski, S. M., Pych, W., Stachowski, G., Krzeminski, W., & Burley, G. S. 2007, *AJ*, 134, 541
- Kaluzny, J., Wysocka, A., Stanek, K. Z., & Krzeminski, W. 1998, *ACTAA*, 48, 439
- Kilic, M., von Hippel, T., Leggett, S. K., & Winget, D. E. 2006, *ApJ*, 646, 474
- Kilic, M., Farihi, J., Nitta, A., & Leggett, S. K. 2008, *AJ*, 136, 111
- Koester, D., Rollenhagen, K., Napiwotzki, R., oss, B., Christlieb, N., Homeier, D., & Reimers, D. 2005, *A&A*, 432, 1025
- Liebert, J., Bergeron, P., & Holberg, J. B. 2005, *ApJS*, 156, 47
- Marín-Franch, A., Aparicio, A., Piotto, G., Rosenberg, A., Chaboyer, B., Sarajedini, A., Siegel, M., Anderson, J., Bedin, L. R., Dotter, A., Hempel, M., King, I., Majewski, S., Milone, A. P., Paust, N., & Reid, I. N. 2009, *ApJ*, 694, 1498
- McCook, G. P. & Sion, E. M. 1999, *ApJS*, 121, 1
- McLaughlin, D. E., Anderson, J., Meylan, G., Gebhardt, K., Pryor, C., Minniti, D., & Phinney, S. 2006, *ApJS*, 166, 249
- Moehler, S., Koester, D., Zoccali, M., Ferraro, F. R., Heber, U., Napiwotzki, R., & Renzini, A. 2004, *A&A*, 420, 515
- Monelli, M., Cassisi, S., Bernard, E. J., Hidalgo, S. L., Aparicio, A., Gallart, C., & Skillman, E. D. 2010, *ApJ*, 718, 707
- Paquette, C., Pelletier, C., Fontaine, G., & Michaud, G. 1986, *ApJS*, 61, 197
- Percival, S. M., Salaris, M., van Wyk, F., & Kilkeny, D. 2002, *ApJ*, 573, 174
- Probst, R. G. 1983, *ApJS*, 53, 335
- Reid, N. 1998, *AJ*, 115, 204
- Renzini, A. & Fusi Pecci, F. 1988, *ARA&A*, 26, 199
- Renzini, A., Bragaglia, A., Ferraro, F. R., Gilmozzi, R., Ortolani, S., Holberg, J. B., Liebert, J., Wesemael, F., & Bohlín, R. C. 1996, *ApJ*, 465, L23
- Richer, H. B., Brewer, J., Fahlman, G. G., Gibson, B. K., Hansen, B. M., Ibata, R., Kalirai, J. S., Limongi, M., Rich, R. M., Saviane, I., Shara, M. M., & Stetson, P. B. 2002, *ApJ*, 574, L151
- Richer, H. B., Dotter, A., Hurley, J., Anderson, J., King, I., Davis, S., Fahlman, G. G., Hansen, B. M. S., Kalirai, J., Paust, N., Rich, R. M., & Shara, M. M. 2008, *AJ*, 135, 2141
- Salaris, M., Held, E. V., Ortolani, S., Gullieuszk, M., & Momany, Y. 2007, *A&A*, 476, 243
- Salaris, M. & Weiss, A. 1998, *A&A*, 335, 943

- Spiegel, D. N., Verde, L., Peiris, H. V., Komatsu, E., Nolte, M. R., Bennett, C. L., Halpern, M., Hinshaw, G., Jarosik, N., Kogut, A., Limon, M., Meyer, S. S., Page, L., Tucker, G. S., Weiland, J. L., Wollack, E., & Wright, E. L. 2003, *ApJS*, 148, 175
- Storm, J., Nordstrom, B., Carney, B. W., & Anderson, J. 1994, *A&A*, 291, 121
- Thompson, I. B., Kaluzny, J., Rucinski, S. M., Krzeminski, W., Pych, W., Dotter, A., & Burley, G. S. 2010, *AJ*, 139, 329
- Tremblay, P.-E. & Bergeron, P. 2008, *ApJ*, 672, 1144
- Tremblay, P.-E., Bergeron, P., & Gianninas, A. 2011, *ApJ*, 730, 128
- von Hippel, T., Kuchner, M. J., Kilic, M., Mullally, F., & Reach, W. T. 2007, *ApJ*, 662, 544
- Woodley, K. A. et al. 2012, in preparation
- Zoccali, M., Renzini, A., Ortolani, S., Bragaglia, A., Bohlin, R., Carretta, E., Ferraro, F. R., Gilmozzi, R., Holberg, J. B., Marconi, G., Rich, R. M., & Wesemael, F. 2001 *ApJ*, 553, 733
- Zoccali, M., Cassisi, S., Piotto, G., Bono, G., & Salaris, M. 1999, *ApJ*, 518, L49
- Zuckerman, B. & Becklin, E. E. 1987a, *ApJ*, 319, L99
- Zuckerman, B. & Becklin, E. E. 1987b, *ApJ*, 330, L138
- Zuckerman, B., Koester, D., Reid, I. N., & Hünsch, M. 2003, *ApJ*, 596, 477
- Zuckerman, B., Melis, C., Klein, B., Koester, D., & Jura, M. 2010, *ApJ*, 722, 725

TABLE 2
DATA ON THE SELECTED WHITE DWARFS

ID	Field	<i>R.A.</i> (J2000)	<i>Decl.</i> (J2000)	F390W (mag)	σ_{F390W} (mag)	F606W (mag)	σ_{F606W} (mag)	F110W (mag)	σ_{F110W} (mag)	F160W (mag)	σ_{F160W} (mag)	T_{eff}^a (K)	$\sigma_{T_{\text{eff}}}$ (K)
WD 1	Swath 1	00:22:40.912	-72:10:32.52	25.396	0.0351	25.362	0.0320	25.500	0.1301	25.515	0.2238	12047	1602
WD 2	Swath 1	00:22:25.686	-72:10:11.84	23.620	0.0207	23.950	0.0194	24.473	0.0464	24.430	0.0705	20698	1361
WD 3	Swath 2	00:21:57.095	-72:10:18.59	24.263	0.0223	24.381	0.0213	24.866	0.0623	24.898	0.1030	16132	1041
WD 4	Swath 2	00:22:00.123	-72:10:12.02	24.399	0.0163	24.495	0.0182	24.722	0.0566	24.732	0.0987	14570	720
WD 5	Swath 2	00:22:00.719	-72:09:15.09	25.217	0.0270	25.125	0.0322	25.303	0.0763	25.297	0.1365	11687	1161
WD 6	Swath 2	00:22:26.133	-72:09:20.01	24.108	0.0134	24.287	0.0235	24.633	0.0612	24.631	0.1141	16372	921
WD 7	Swath 2	00:22:01.506	-72:08:34.31	23.314	0.0220	23.684	0.0153	24.070	0.0386	24.062	0.0683	20458	1281
WD 8	Swath 2	00:22:25.423	-72:09:09.83	25.257	0.0338	25.138	0.0316	25.325	0.0828	25.373	0.1618	11566	1281
WD 9	Swath 2	00:22:23.633	-72:09:00.06	23.728	0.0242	24.001	0.0305	24.552	0.0550	24.795	0.1454	20257	1722
WD 10	Swath 3	00:21:31.487	-72:08:35.91	23.950	0.0213	24.129	0.0239	24.624	0.0618	24.996	0.1379	17574	1201
WD 11	Swath 3	00:21:39.401	-72:09:03.65	25.658	0.0271	25.498	0.0292	25.538	0.1380	25.140	0.2300	9684	1041
WD 12	Swath 3	00:21:51.751	-72:09:31.15	24.491	0.0146	24.527	0.0143	24.726	0.0558	24.953	0.1187	13889	640
WD 13	Swath 3	00:22:01.247	-72:09:16.43	25.190	0.0318	25.088	0.0218	25.168	0.0731	25.056	0.1274	10966	961
WD 14	Swath 3	00:21:47.243	-72:08:22.44	25.310	0.0232	25.168	0.0257	25.292	0.0747	24.953	0.0945	10285	640
WD 15	Swath 3	00:21:47.989	-72:08:15.89	25.613	0.0291	25.463	0.0316	25.542	0.0982	25.239	0.1113	10045	801
WD 16	Swath 3	00:21:41.681	-72:07:49.43	24.062	0.0179	24.265	0.0182	24.778	0.0581	24.658	0.0921	17374	1001
WD 17	Swath 3	00:21:42.075	-72:07:47.08	24.640	0.0263	24.711	0.0233	25.057	0.0772	25.144	0.1618	14730	1041
WD 18	Swath 3	00:21:46.162	-72:07:54.27	23.548	0.0210	23.877	0.0178	24.352	0.0638	24.332	0.0914	19977	1401
WD 19	Swath 3	00:22:02.034	-72:08:35.65	23.332	0.0215	23.688	0.0191	24.209	0.0448	24.371	0.0739	22220	1481
WD 20	Swath 3	00:21:53.267	-72:08:02.38	24.810	0.0203	24.744	0.0225	25.257	0.0831	25.381	0.2374	13048	961
WD 21	Swath 4	00:21:30.986	-72:08:00.98	24.132	0.0257	24.272	0.0247	24.622	0.0529	24.548	0.0971	15812	1041
WD 22	Swath 5	00:21:07.243	-72:04:31.54	24.833	0.0275	24.712	0.0213	25.087	0.0823	24.955	0.1090	12207	1001
WD 23	Swath 5	00:21:15.803	-72:06:00.35	24.392	0.0309	24.438	0.0261	24.956	0.0803	24.806	0.1638	14971	1201
WD 24	Swath 5	00:21:17.805	-72:04:23.82	23.039	0.0199	23.469	0.0151	24.030	0.0558	23.951	0.0668	23221	1401
WD 25	Swath 5	00:21:23.488	-72:03:44.75	23.803	0.0237	24.057	0.0245	24.460	0.0606	24.654	0.0875	18816	1361
WD 26	Swath 5	00:21:32.257	-72:05:38.40	22.316	0.0209	22.940	0.0134	23.570	0.0345	23.641	0.0564	31712	2563
WD 27	Swath 6	00:21:26.729	-72:01:40.22	25.413	0.0376	25.337	0.0198	25.266	0.0843	25.044	0.1158	9924	841
WD 28	Swath 6	00:21:23.115	-72:03:44.39	23.816	0.0156	24.088	0.0360	24.429	0.0449	24.652	0.0810	18655	1121
WD 29	Swath 7	00:21:39.901	-71:59:46.59	24.809	0.0260	24.789	0.0226	25.096	0.0698	25.418	0.1630	13569	1041
WD 30	Swath 7	00:21:31.482	-72:01:05.77	24.259	0.0117	24.505	0.0125	24.822	0.0581	25.031	0.0938	17614	720
WD 31	Swath 7	00:21:48.558	-72:00:42.08	23.079	0.0356	23.569	0.0165	24.071	0.0388	24.183	0.0619	25544	2242
WD 32	Swath 8	00:21:55.432	-71:58:34.17	24.546	0.0294	24.549	0.0256	24.842	0.0576	24.642	0.0772	13329	1041
WD 33	Swath 8	00:22:00.315	-71:58:30.80	25.161	0.0322	25.080	0.0281	25.279	0.0724	24.927	0.0880	11086	961
WD 34	Swath 8	00:21:59.219	-71:58:45.40	25.135	0.0303	25.140	0.0240	25.094	0.0649	25.171	0.1203	11246	1121
WD 35	Swath 8	00:21:57.370	-71:59:11.32	22.845	0.0233	23.291	0.0186	23.843	0.0332	23.997	0.0509	25584	1642
WD 36	Swath 8	00:22:05.843	-71:59:28.07	24.740	0.0295	24.749	0.0277	24.944	0.0686	24.924	0.1045	13209	1161
WD 37	Swath 9	00:22:21.111	-71:57:49.36	23.525	0.0305	23.832	0.0247	24.309	0.0454	24.645	0.0911	21419	1802
WD 38	Swath 9	00:22:12.785	-71:58:54.71	25.127	0.0260	25.015	0.0220	25.241	0.0781	25.100	0.1078	11446	961
WD 39	Swath 10	00:22:55.003	-71:57:27.72	24.810	0.0188	24.749	0.0178	25.060	0.0700	25.658	0.1799	12888	881
WD 40	Swath 10	00:22:59.788	-71:57:41.86	25.047	0.0274	24.976	0.0250	25.020	0.0647	24.961	0.1094	11006	881
WD 41	Swath 10	00:22:36.414	-71:57:47.74	24.791	0.0306	24.775	0.0284	24.988	0.0719	25.118	0.1012	13409	1161
WD 42	Swath 10	00:22:56.251	-71:57:55.80	22.920	0.0167	23.420	0.0225	23.819	0.0340	23.777	0.0557	23461	1201
WD 43	Swath 10	00:22:33.763	-71:58:55.87	25.673	0.0391	25.548	0.0274	25.462	0.0908	25.290	0.1584	9804	921
WD 44	Swath 11	00:22:59.738	-71:57:42.01	25.090	0.0386	25.060	0.0247	25.160	0.0726	25.228	0.2013	11927	1441
WD 45	Swath 12	00:23:33.344	-71:58:26.77	24.259	0.0177	24.387	0.0193	24.446	0.0725	24.447	0.1015	14690	801
WD 46	Swath 12	00:23:26.967	-71:58:57.50	23.188	0.0194	23.617	0.0193	24.063	0.0596	24.366	0.1228	23141	1561
WD 47	Swath 12	00:23:32.372	-71:59:45.70	22.430	0.0133	23.026	0.0158	23.507	0.0376	23.823	0.0538	29509	1762
WD 48	Swath 12	00:23:21.810	-71:59:18.03	24.233	0.0179	24.376	0.0250	24.915	0.0882	25.064	0.1247	16653	1121
WD 49	Swath 12	00:23:37.390	-72:00:36.89	23.387	0.0151	23.753	0.0208	24.122	0.1033	24.002	0.1056	20017	1361
WD 50	Swath 12	00:23:28.612	-72:00:43.42	24.186	0.0227	24.289	0.0250	24.459	0.0823	24.690	0.1327	14770	1001
WD 51	Stare	00:23:32.099	-72:09:39.30	23.982	0.0346	24.166	0.0248	24.569	0.0471	24.632	0.2060	17254	1481
WD 52	Stare	00:23:00.862	-72:10:38.40	25.293	0.0497	25.221	0.0258	25.361	0.0681	25.014	0.0842	10725	921
WD 53	Stare	00:23:17.641	-72:09:53.81	25.215	0.0370	25.103	0.0244	25.282	0.0706	25.734	0.2999	11687	1281
WD 54	Stare	00:23:09.435	-72:10:11.30	23.998	0.0178	24.209	0.0172	24.527	0.0241	24.668	0.0740	16973	760
WD 55	Stare	00:23:18.825	-72:09:08.07	23.725	0.0201	24.025	0.0175	24.597	0.0727	24.505	0.0780	19416	1241
WD 56	Stare	00:23:12.136	-72:09:23.12	25.264	0.0520	25.184	0.0252	25.310	0.0333	25.692	0.1589	12047	1081
WD 57	Stare	00:23:03.033	-72:09:05.57	25.514	0.0426	25.467	0.0291	25.430	0.0524	25.235	0.1018	10325	720
WD 58	Stare	00:23:13.822	-72:08:18.48	23.385	0.0147	23.794	0.0198	24.341	0.0291	24.294	0.0418	23341	1001
WD 59	Stare	00:22:55.764	-72:08:56.88	22.639	0.0105	23.219	0.0159	23.758	0.0129	23.890	0.0262	29028	801

^a Effective temperature estimates assume a white dwarf mass of 0.53 M_{\odot} .

Fig. Set 3. Images of our WD sample

Fig. Set 6. Spectral Energy Distributions and likelihood fits for our WDs